UHASSELT
KNOWLEDGE IN ACTION

Maastricht University

Faculty of Medicine and Life Sciences
School for Life Sciences
Master of Biomedical Sciences

Master's thesis

Optimization of the histological and immunohistological approach to investigate tumor heterogeneity in non-small cell lung cancer

Chiara Derickx

Thesis presented in fulfillment of the requirements for the degree of Master of Biomedical Sciences, specialization Molecular Mechanisms in Health and Disease

SUPERVISOR :

Prof. dr. Esther WOLFS

MENTOR :

Mevrouw Kim NIJSTEN

2022
2023

Transnational University Limburg is a unique collaboration of two universities in two countries: the University of Hasselt and Maastricht University.

UHASSELT
KNOWLEDGE IN ACTION

www.uhasselt.be
Universiteit Hasselt
Campus Hasselt:
Martelarenlaan 42 | 3500 Hasselt
Campus Diepenbeek:
Agoralaan Gebouw D | 3590 Diepenbeek

Faculty of Medicine and Life Sciences
School for Life Sciences
Master of Biomedical Sciences

Master's thesis

Optimization of the histological and immunohistological approach to investigate tumor heterogeneity in non-small cell lung cancer

Chiara Derickx

Thesis presented in fulfillment of the requirements for the degree of Master of Biomedical Sciences, specialization Molecular Mechanisms in Health and Disease

SUPERVISOR :

Prof. dr. Esther WOLFS

MENTOR :

Mevrouw Kim NIJSTEN

Optimization of the histological and immunohistological approach to investigate tumor heterogeneity in non-small cell lung cancer*

Chiara Derickx.[1], Kim Nijsten[1], and Esther Wolfs[1]

[1]Lab for Functional Imaging & Research on Stem Cells (FIERCE Lab), Cardio and organ systems research group, Biomedical Research Institute, Universiteit Hasselt, Campus Diepenbeek, Agoralaan Gebouw C - B-3590 Diepenbeek

*Running title: *Optimization staining procedures for digitization*

To whom correspondence should be addressed: Wolfs Esther, Tel: +3211269296; Email: esther.wolfs@uhasselt.be

Keywords: non-small cell lung cancer, spatial tumor heterogeneity, histology, immunohistochemistry, digital pathology

ABSTRACT

Lung cancer causes the most cancer-related deaths worldwide, whereby its subtype, non-small cell lung cancer (NSCLC), affects the most patients. Lung cancer treatment often fails due to late and insufficient tumor detection. Furthermore, spatial tumor heterogeneity has an effect on the treatment response. Insight into potential differences in spatial tumor heterogeneity can be assessed using histological and immunohistochemistry (IHC) approaches. Therefore this study re-evaluated and optimized the histological and IHC staining process aiming to acquire the highest quality images when digitizing these stained tissue slides. All experiments were performed on healthy murine tissue pending the tumor tissue obtained from the Kras/Lkb1 mouse model. First, several cell-specific makers, such as CK7 (epithelial component) and CD34 (blood vessels), were assessed to map the tumor and its microenvironment. Secondly, the clearing agents NeoClear and UltraClear, safer alternatives for Xylene, were studied. Xylene, NeoClear, and UltraClear were compared based on (1) hematoxylin and eosin (H&E), (2) Masson's trichrome (TCM), (3) 3,3'-diaminobenzidine (DAB)-based IHC, as well as (4) immunofluorescent analysis. All stained tissue slides were visualized using whole-slide imaging. At this moment, no conclusions can be made for the comparison of different clearing agents based on the used staining techniques. Furthermore, implementing additional markers, which visualize other tumor-associated cells, will allow the mapping of the entire tumor microenvironment in future research. In summary, further optimization of the clearing agents and the implementation of other cell-specific markers are necessary to gain insight into spatial tumor heterogeneity.

INTRODUCTION

Lung cancer

Prevalence and risk factors – Lung cancer is the global leading cause of all cancer-related deaths. In 2020, this accounted for about 1.8 million deaths worldwide [1-3]. In Belgium, lung cancer is responsible for the most deaths before the age of 75 [4]. Furthermore, it is the most frequently diagnosed cancer; it accounts for approximately 12.4% of all cancer diagnoses [1, 2]. Several risk factors play a role in the development of lung cancer, such as smoking, radiation, air pollution, and exposure to metals and asbestos. Smoking is the principal risk factor contributing to lung cancer development. [1, 5]. In a complex interplay with environmental factors, it accounts for approximately 90% of all cases. Moreover, inhaling second-hand smoke increases the risk of lung cancer by about 20 to 30% [2, 6]. Additionally, genetic factors can also play a role in lung cancer development [2, 7]. Mutations in several genes, such as Kirsten rat sarcoma (*Kras*) or liver kinase B1 (*Lkb1*), can affect protein synthesis leading to a disruption in the cell cycle and the start of the carcinogenic process [2, 8]. Although different risk factors can

be associated with lung cancer development, the pathophysiology remains poorly understood.

Subtypes – Lung cancer encompasses two main types: small cell lung cancer (SCLC) and non-small cell lung cancer (NSCLC). SCLC develops in the central airway and is characterized by a disruption of DNA repair mechanisms, resulting in rapid tumor progression [9]. NSCLC, on the other hand, is the least aggressive form and is hallmarked by enlarged cancer cells compared to SCLC. Additionally, a slower growth pattern is observed in NSCLC [10]. This study will focus on NSCLC, which affects about 85% of all lung cancer patients [2]. NSCLC derives from the epithelial cells of the central bronchi towards the terminal alveoli, which can develop into different subtypes of NSCLC. These subtypes are correlated with the site of origin and are classified into adenocarcinoma (ADC, lung periphery, ~48%), squamous cell carcinoma (SCC, central lung or bronchi, ~28%), and large cell carcinoma (LCC, lung periphery or central lung, ~24%) [1, 9, 11-14]. Within this research, the focus will be on ADC and SCC and their intermediate form, adenosquamous cell carcinoma (ADSCC) (**Fig. 1**) [10]. These different forms can be distinguished based on histological features [1]. More specifically, ADC arises from epithelial cells in the bronchial glands and represents different growth patterns, including a lepidic, acinar, papillary, micropapillary, and solid pattern. Lepidic refers to mucinous and nonmucinous tumor cells along alveolar walls, whereas acinar is tumor tissue arranged in tubules and consists of cuboidal cells resembling epithelial cells of mucosal glands. The papillary and micropapillary growth pattern refers to bigger or small papillae structures. Lastly, closely packed tumor cells are observed in the solid type [5, 15]. Furthermore, ADC is the most prevalent form in non-smokers [5, 16]. In contrast to ADC, SCC often develops in the central part of the lung or the bronchi. In this subtype, the squamous cells, which are flat cells lining organs, are affected. In this case, smoking is the main cause of cellular transformation. Moreover, SCC also shows intercellular bridges and keratinization, including the formation of keratin pearls [17, 18]. Lastly, the ADSCC has histological characteristics from both the ADC and SCC. Since biopsies mostly contain only features from either ADC or SCC, diagnosis of this mixed form is challenging. Furthermore, the tumor is only classified as ADSCC when each component contains at least 10% of ADC and SCC, according to the World Health Organisation classification. Besides, the very low incidence of ADSCC, it is an aggressive form of NSCLC with a poor prognosis [10].

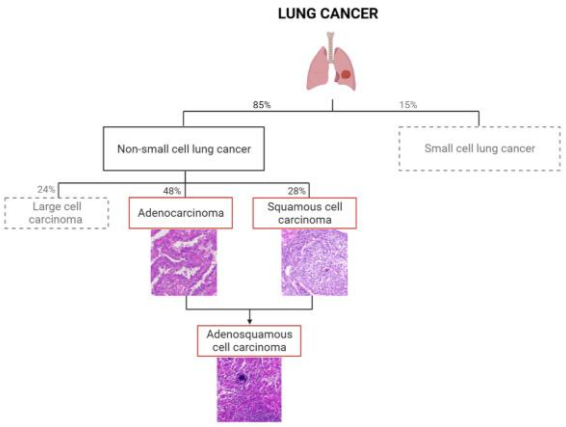

Fig. 1 – Lung cancer classification. Lung cancer is classified into two main subtypes: non-small cell lung cancer (NSCLC) and small cell lung cancer, whereby NSCLC affects 85% of all patients. Moreover, NSCLC can be subdivided into three types: adenocarcinoma (ADC), squamous cell carcinoma (SCC), and large cell carcinoma. This research focuses on the ADC and SCC. A mixed form of these types, referred to as adenosquamous cell carcinoma, is also included. *Figure made in BioRender.*

Diagnosis and current therapies – Although there are different subtypes of NSCLC, their treatment plan is similar and includes surgery, radiotherapy, chemotherapy, immunotherapy, or targeted therapy [12, 19]. Despite these several therapy options, lung cancer treatment often fails due to late and insufficient detection and diagnosis of the tumor. Lung cancer is diagnosed via several imaging tests, such as computed tomography scans, sputum cytology, and biopsy analysis [20]. At this moment, hematoxylin and eosin (H&E) staining is used as a gold standard in hospitals to diagnose lung cancer in tumor biopsies. Additionally, a panel of markers can be used to validate the diagnosis [21, 22]. Thyroid transcription factor (TTF1) and cytokeratin 7 (CK7) are markers for epithelial cells, indicating ADC. TTF1 plays an essential role in the morphogenesis of the healthy lung, but also in lung cancer. It influences the growth of tumor cells and their metastasis via downstream genes

such as the epidermal growth factor receptor (*EGFR*)[23, 24]. CK7 is coexpressed during the proliferation and differentiation of stratified epithelial tissue indicating its role in cancer development [25, 26]. To distinguish SCC, P40 and P63, which indicate epithelial cells, were visualized [22, 27]. The growth and development of ectoderm structures, specifically myoepithelial cells, are shown by P63 [27]. Furthermore, overexpression of P63 in stratified squamous epithelium leads to cell proliferation and survival. Additionally, apoptotic and senescence processes are inhibited [28]. A P63 isoform, P40, also indicates epithelial cells in SCC. This isoform is also involved in proliferation and differentiation but shows a higher sensitivity and specificity for SCC than P63 [22]. Nevertheless, biopsy analyses are labor-intensive and time-consuming. Therefore, this research project aims to facilitate this diagnostic process and establish a more accurate diagnosis and treatment plan by studying tumor heterogeneity as a potential biomarker.

Tumor heterogeneity

Definition and types – One of the ongoing challenges within drug development and lung cancer treatment is tumor heterogeneity, referring to a broad spectrum of differences within the tumor microenvironment [29, 30]. Tumor heterogeneity affects cancer development, progression, and evolution. Furthermore, Wu et al. described that tumor heterogeneity influences the survival of patients suffering from ADC [31, 32]. The first type of heterogeneity is intertumoral heterogeneity, which indicates the tumor microenvironment differences between cancer patients. In contrast, intratumoral heterogeneity refers to the variations of cell types within one tumor [33]. Another form of heterogeneity is temporal tumor heterogeneity, which includes the evolution of the tumor over time. Furthermore, spatial tumor heterogeneity is referred to the difference in cell types and their organization within the tumor microenvironment. Various cell types, such as tumor cells, endothelial cells, neurons, etc., can be present within this microenvironment [34]. This research aims to gain insight into the spatial tumor heterogeneity of NSCLC subtypes. Mapping of this spatial tumor heterogeneity can, among others, be assessed using histological and immunofluorescent (IF) approaches [31, 35].

Assessment of the spatial tumor heterogeneity – Here, histological stainings provide an overview of the cell morphology in the tissue. This is important since the cell morphology degrades when using IF-based staining methods to map the tumor. As mentioned above, various markers are used to distinguish cancer subtypes. However, other cell types must be included to acquire total overview of the tumor and its microenvironment. For example, pancytokeratin detects a panel of different CKs in various epithelia of different tumors [36]. Moreover, tumors that did not derive from epithelial cells are more likely negative for pancytokeratin [37]. Furthermore, vascularization plays an essential role in tumor growth and metastasis. More specifically, this process ensures tumor cells to be provided with nutrients, oxygen, and growth factors. These vascular structures can be visualized by CD34, a transmembrane phosphoglycoprotein of vascular endothelial cells . It is suggested that CD34 has a role in cell adhesion, cell differentiation, and proliferation [38-40]. Besides blood vessels, nerves can also play a role in the metastatic spreading of the tumor [40]. Markers, such as beta 3-tubulin, can specify neurons due to its role in neuronal differentiation [41]. Furthermore, lymph vessels and nodes are the initial sites of cancer metastasis. To map these vessels, podoplanin, a transmembrane receptor glycoprotein expressed in the lymphatic endothelium of normal tissue, can be used [42, 43].

Currently, both histological and immunohistochemical (IHC) methods are essential for the characterization of spatial tumor heterogeneity using digital pathology. Re-evaluation of these staining methods is crucial to obtain an optimal protocol for digitization. Different steps must be performed before executing histological and IHC stainings on the tissue of interest. First, fixation is conducted to preserve and protect the tissue structure from degradation. Afterward, water needs to be extracted by dehydrating agents, like ethanol, to harden the tissue. The next essential step of tissue processing involves embedding [44]. Here, a clearing agent prepares the tissue for impregnation with paraffin [45]. Finally, the tissue can be sliced and placed on a glass slide to start staining [44]. The tissue must be deparaffinized with clearing agents that remove paraffin to perform stainings. [45]. The most widely used clearing agent is Xylene. Xylene is

carcinogenic and toxic, which can result in irritation of the eyes, skin, and respiratory tract. Furthermore, it can also cause unconsciousness and possible death due to respiratory failure [45]. Therefore, safer alternatives such as NeoClear and UltraClear are emerging. Previous research by Alwahaibi et al. showed that UltraClear, which is less toxic and harmful to the environment, has promising deparaffinized and pre-embedding properties. However, further studies are necessary [45, 46]. NeoClear is another alternative clearing agent. This product evaporates more difficult than Xylene, resulting in less health hazards [47]. In addition to these histological and IHC approaches, other research groups used mass spectrometry or sequencing methods to determine tumor heterogeneity [32]. However, since this research aims to gain insights into spatial tumor heterogeneity, the focus will be on the previously mentioned staining techniques.

Preclinical mouse model

The Kras/Lkb1 mouse model to investigate NSCLC – To investigate the spatial tumor heterogeneity of different NSCLC subtypes, at first a preclinical mouse model is used due to the preciousness and high variability of human tumor samples. The Kras/Lkb1 mouse model recapitulates the NSCLC pathology elegantly. More specifically, this transgenic mouse model reproduces all different subtypes of NSCLC. It demonstrates nicely the transdifferentiation of ADC towards SCC with ADSCC as the mixed subtype. This intermediate form is also observed in human lung cancer pathology [48]. Furthermore, the Kras/Lkb1 mouse model harbors two genes that also play a role in human lung cancer development [2, 49]. *Kras* is a frequently mutated proto-oncogene in NSCLC and regulates cell growth, proliferation, and survival via downstream signaling of the RAF/MEK/ERK pathway [50]. Consequently, mutations of *Kras* will lead to excessive cell proliferation and aid in this way in the development of lung cancer. This mutation is mainly observed in the ADC subtype [49]. However, this mutation can also occur in lower levels in the SCC class [49-51]. Several *Kras* mutations are present in lung cancer, such as $Kras^{G12C}$, $Kras^{G12V,}$ and $Kras^{G12D}$ [52]. This study focuses on the heterozygous $Kras^{G12D}$ ($Kras^{G12D+/-}$) mutation [48, 52, 53]. Another common genetic alteration, present in about one-third of NSCLCs, is the mutation in the liver kinase B1 (*Lkb1*) gene. A loss-of-function mutation in this tumor suppressor gene will result in complications with cell polarity and energy metabolism [11, 48, 54, 55]. Moreover, tumors with *Lkb1* deficiency have rapid cell proliferation and are more likely to metastasize because angiogenesis is stimulated via the vascular endothelial growth factor (VEGF) pathway [54, 56]. *Lkb1* mutations are observed in lung cancer patients with ADC, SCC, or ADSCC [11]. Previous research by Han et al. showed that homozygous *Lkb1*-deficiency ($Lkb1^{-/-}$) in mice accelerates cancer progression [11, 48]. Another advantage of this mouse model is that it allows the implementation of the Cre-Lox recombinase system [57].

Cre-Lox recombinase system – The Cre-Lox system is able to manipulate the DNA in a specific manner. Here, Cre-recombinase causes the recombination of two LoxP sites. This action results in either gene activation, leading to a heterozygous $Kras^{G12D+/-}$ mutation and gene inactivation via the homozygous $Lkb1^{-/-}$ deletion [11, 57, 58]. The Cre-Lox recombinase system allows one to choose the time point of the tumor induction. Furthermore, Ji et al. described a clear indication of the specific time at which ADC, ADSCC, and SCC pathophysiology can be studied in Kras/Lkb1 mouse model. This would occur respectively at eight weeks, between eight and ten weeks, and ten weeks post-tumor induction [11, 57].

Digital pathology

Pathology is important in drug discovery and translational and clinical research programs. It is also involved in disease classification, as seen in lung cancer diagnosis. These traditional pathology techniques, such as histological and IHC approaches, have a low cost and high availability [59]. However, variations in staining methods between different laboratories and interpretation of the results remain challenging. This can lead to inconsistent diagnosis, which can influence the treatment plan of a patient. Therefore, digital pathology is a widespread emerging field in research and hospitals, since it improves efficiency of the pathological workflow [59]. Digital pathology includes various steps such as whole-slide imaging (WSI) and generation of artificial intelligence (AI) tools [60]. These tools will allows us to study a biomarker, like spatial tumor heterogeneity [59]. Furthermore, reduced variability in treatment plans and implementation of a faster and more accurate treatment plan in a shorter time period

are potential advantages using digital pathology [60]. Digitization of a tissue slide will provide a lot of information about the histological features, like cell morphology or cell types, since this provides a complete overview of the tissue slide [59, 60]. The aim of this research is the digitization of samples via WSI to generate a complete overview of the tissue slide. This allows studying the spatial tumor heterogeneity. However, to achieve digitized tissue slides, it is crucial to have an optimal staining procedure that is suitable for WSI.

This research will optimize the histological and IF staining process since an optimal staining procedure is required for the digitization of tissue slides. First, different cell-specific markers will be tested using immunohistochemistry approaches. Both the 3,3'-diaminobenzidine (DAB)-based technique and the IF analysis will be performed. Next to specific markers, also an high quality clearing agent is necessary for optimal staining results. Here, hematoxylin and eosin (H&E) staining, visualizing the cell morphology, is used to compare different clearing agents. Additionally, a Masson's Trichrome (TCM) staining and immunohistochemistry will be performed. An optimal staining protocol, whereby stained slides can be digitized using WSI, is aimed to achieve. The optimization of these procedures as well as its digitization protocol will pave the way toward the establishment of the potential tumor heterogeneity profile of the different NSCLC subtypes.

EXPERIMENTAL PROCEDURES

Preclinical mouse model

Animal breeding and housing – The *Kras*$^{G12D+/-}$/*Lkb1*$^{-/-}$ breeding line was granted by Prof. Dr. Grit Herter-Sprie (University of Cologne, Germany) and bred in-house (Biomed, Hasselt University, Belgium) (**Fig S. 1**) [57]. All mice were housed in an automatic 12:12 hour light:dark cycle. Furthermore, a standardized temperature between 20°C and 24°C and relative humidity between 40% and 60% was applied. They received drinking water and food pellets at libidum. All animal experiments were performed according to the guidelines and were approved by the Ethische Commisie Dierproeven of Hasselt University.

Genotyping – To select the mice with the correct genotype (*Kras*$^{G12D+/-}$/*Lkb1*$^{-/-}$), their genotype was determined using the KAPA Kit (KK7151-SIAL, Sigma-Aldrich) following the manufacturer's protocol. Ear cuts were taken to collect a DNA sample of each mouse. Different primers were designed for *Kras* and *Lkb1* (**Table 1**). Furthermore, for *Lkb1*, two primer mixes were used. Lkb1 primer mix 1 determines whether this gene is homozygous (600 base pair, bp), heterozygous (200 bp and 600 bp) or wild type (WT; 200 bp). Additionally, Lkb1 primer mix 2 indicates whether the sample is WT or mutant (200-300 bp). For *Kras* and *Lkb1*, different PCR protocols were performed (**Table 1**).

Table 1 – Overview of the primers mixes, PCR protocol and expected outcomes to determine the genotype of the Kras/Lkb1 mouse model.

	Kras	Lkb1 primer mix 1	Lkb1 primer mix 2
Foward primer (5' – 3')	TCCGAATTCA GTGACTACAG ATG	GAGATGGGTA CCAGGAGTTG GGGC	GAGATGGGTA CCAGGAGTTG GGGC
Reverse primer (5' – 3')	CTAGCCACCA TGGCTTGAGT	GGGCTTCCTC CTGGTGCCAG CCTGT	TCTACCAACAA TGCGCTCATCG TCATCCTCGGC
PCR protocol	**1.** 94°C – 30 s **2.** 94°C – 30 s **3.** 64°C – 30 s **4.** 72°C – 1 min **5.** 33x step 2-4 **6.** 72°C – 10 min **7.** 4°C - ∞	**1.** 94°C – 30 s **2.** 94°C – 30 s **3.** 72°C – 45 s **4.** 72°C – 1 min **5.** 33x step 2-4 **6.** 72°C – 10 min **7.** 4°C - ∞	**1.** 94°C – 30 s **2.** 94°C – 30 s **3.** 72°C – 45 s **4.** 72°C – 1 min **5.** 33x step 2-4 **6.** 72°C – 10 min **7.** 4°C - ∞
Outcome	350 bp	600 bp	200 – 300 bp

bp, base pair; Kras, Kirsten rat sarcoma; Lkb1, Liver kinase B1; PCR, Polymerase chain reaction.

Tumor induction – The tumors were induced as described by DuPage et al. [61]. Female and male *Kras*$^{G12D+/-}$/*Lkb1*$^{-/-}$ mice were anesthetized using a Nimatek (ketamine; 80 mg/kg)/Rompun (xylazine; 10 mg/kg) solution. A total dose of 5 µl/g body weight was injected intraperitoneally. When the whisker reflex was absent, a solution with calcium (10mM; $CaCl_2$; C1016 Sigma-Aldrich), minimal essential medium (MEM, M4655, Sigma-Aldrich), and Ad5CMVCre (2 x 10^6 pfu/µl; Viral Vector Core University of Iowa) (Ad-Cre) was administered intranasally. This Ad-Cre solution was incubated 20 to 30 min prior to administration to allow precipitate formulation. A total amount of 40 µl Ad-Cre solution, distributed in smaller droplets, was inhaled by each mouse (**Fig S. 1**). The health of the mice was observed daily, whereas the tumor growth was monitored by weekly body weight measurements.

Stainings

Immunohistochemistry – Healthy lung tissue and tissue from the kidney, prostate, and colon as positive control tissue were obtained from surplus mice and fixated for 24h with 4% paraformaldehyde (PFA, 4°C). Next, the tissue was embedded in paraffin using the following protocol:

1. 2 x 75% ethanol – 1 h
2. 2 x 95% ethanol – 1 h
3. 3 x 100% ethanol – 1h
4. 2 x Clearing – 1h
5. Paraffin 1 – 2h
6. Paraffin 2 – 3h

Tissue sections of 4 µm were obtained using the microtome. All the lung and control tissue was deparaffinized with two times Xylene (5 min), and rehydrated by a serie of decreasing ethanol concentrations (100%, absolute - 100%, denaturated - 100%, denaturated - 95% - 75%), and distilled water (2 min). For the IF-IHC staining, antigen retrieval with citrate buffer was performed to enable access for the primary antibody to the target protein. Furthermore, to avoid non-specific bindings of the antibody, a blocking step with pure protein block (XO-909, DAKO) was performed. Washing steps with 1x phosphate buffered saline (1x PBS) were performed between the different steps. The primary antibody was incubated overnight at 4°C. **Table 2** provides an overview of the primary antibodies to visualize several cell types, such as nerves, epithelial cells, endothelial cells from blood and lymph vessels, stromal cells, and tumor cells. After incubation with the primary antibody, a fluorescent secondary antibody was incubated for 1 h (**Table S. 1**). DAPI was used to counterstain the nuclei. Again several washing steps with 1x PBS were performed. Mounting was accomplished using ProLung Antifade mountant (P36930, Invitrogen).

When performing the DAB-IHC staining, a peroxidase blocking step was used before the primary antibody to block the endogenous peroxidase activity of the tissue (**Table 2**). Subsequently, to primary antibody incubation, the secondary antibody conjugated with horseradish peroxidase (HRP) was added (**Table S. 2**). Afterward, hematoxylin was used as a counterstaining to visualize the cell nuclei. Next, a washing step with tap and distilled water was performed. This was followed by dehydration of the tissue with an increasing serie of ethanol concentrations (75% - 95% - 100%, denaturated - 100%, denaturated - 100%, absolute) 2 min each and Xylene (2 x 5 min). Mounting was performed with dibutylphthalate polystyrene xylene (DPX). All stained tissue slides were visualized using the Axio Scan.Z1 Slide Scanner (ZEISS).

Table 2 – Overview of the used primary antibodies (AB) to visualize specific cell types.

Primary AB	Cell type	Dilution	Reference
Beta 3-tubulin	Neurons	1:300	T8578-200L Sigma-Aldrich
CD34	Epithelium Blood vessels	1:1000	AB81289 Abcam
CK7	Epithelium Marker ADC	1:1000	AB181598 Abcam
P63	Epithelium Marker SCC	1:100	AB735 Abcam
Pancytokeratin (ae1/ae3)	Epithelium	1:50	M3515 DAKO
Podoplanin	Endothelium Lymph vessels	1:7.5	8.1.1 – s DSHB
Vimentin	Stromal cells	1:100	AB5733 Sigma-Aldrich

ADC, adenocarcinoma; CK, cytokeratin; SCC, squamous cell carcinoma.

Tissue processing – Xylene, NeoClear, and UltraClear were compared using H&E, TCM, DAB-IHC, and IF-IHC staining methods on murine lung tissue. Embedding and deparaffinization were similar to the protocol described above, using different clearing agents. After deparaffinization with Xylene, NeoClear, or UltraClear, the slides were incubated in hematoxylin to visualize the nuclei. After several washing steps with tap and distilled water, eosin was used to stain the cytoplasm and extracellular matrix (ECM). This was followed by dehydration of the tissue with a serie of increasing ethanol concentrations (75% - 95% - 100%, denaturated - 100%, denaturated - 100%, absolute) and the clearing agent. Finally, samples deparaffinized in Xylene, NeoClear, and UltraClear were mounted with DPX, Neomount, and Ultrakit, respectively. Furthermore, TCM staining was used to compare the three clearing agents. This staining method distinguishes cells from the surrounding connective tissue. Deparaffinization with a Xylene, NeoClear, or UltraClear was followed by incubation with different stains, specifically hematoxylin to stain the nuclei, ponceau to visualize the cytoplasm and ECM, and aniline blue to specify the connective tissue. Several washing steps with tap or distilled water are performed between these staining steps. Also, phosphomolybdic acid (1%) is used between

these staining steps. Acetic acid (1%) incubated 1 min prior to the dehydration. The slides were dehydrated and mounted, similar to the H&E protocol. Additionally, DAB-IHC and IF-IHC stainings were performed using beta 3-tubulin and podoplanin as markers. All steps are similar to the IF-IHC protocol despite the use of different clearing agents and mounting medium (AntiFade fluorescence mounting medium Abcam, ab104135). All stainings were digitized using the Axio Scan.Z1 Slide Scanner (ZEISS).

Whole-slide imaging: Digitization of human samples

Human NSCLC samples from the PROLUNG study were obtained from Ziekenhuis Oost Limburg (ZOL, Belgium). Both H&E and DAB-IHC tumor tissue samples were provided. All slides were digitized using the Axio Scan.Z1 Slide scanner (ZEISS). The H&E and DAB-IHC slides were digitized using an optimized 40x objective and 20x objective brightfield scanning profile, respectively. These scanned images will be used for further processing with machine learning to develop AI algorithms. This will be enabled through collaboration with the Data Science Institute (DSI) of Hasselt University.

RESULTS

Kras$^{G12D+/-}$*/Lkb1*$^{-/-}$ *mouse model used for tumor induction* – Before the tumor induction procedure, mice with the correct genes (*Kras*$^{G12D+/-}$*/Lkb1*$^{-/-}$) are selected using genotyping. **Fig. 2A** is a representative image of the genotyping results of a mouse that meets the requirements to be included in the tumor induction procedure. The heterozygous LoxP-stop-LoxP flanked *Kras* mutation is observed at 350 base pairs (bp).

Additionally, mice that are selected also need to harbor a double-floxed *Lkb1* gene homozygously. Therefore a band at 600 bp and 200-300 bp is observed for Lkb1 primer mix 1 and 2, respectively. Additionally, to validate the results of the genotyping, three control samples were included: a positive control sample (P) that is known to harbor the genes of interest, a WT, and a no template control (NTC) which lack DNA to ensure the PCR mix is not contaminated. Mice harboring the genotype of interest were used for tumor induction (**Fig. 2B**). The Ad-Cre solution was administered intranasally. After the tumor induction procedure, the health of the animals is monitored by, among other, the assessment of their body weight on a weekly basis. In **Fig. 2C,** the body weight of female (n=8) and male (n=10) mice is shown. Male mice have, in general, a higher body weight compared to female mice. Furthermore, body weight fluctuations are observed, whereby male mice show less fluctuations compared to the female mice in this study. In general, the body weight is stable five weeks post-tumor induction. However, female mouse 6 shows a decrease of 3 g in body weight one week after tumor induction. From week one to two, again, an increase of 3 g in body weight was observed in this mouse. Mice 1 and 4 showed a similar increase in body weight, respectively, between weeks one and two, and weeks two and three post-tumor induction. In all males, a similar body weight is observed, except for male mouse 3, which has a slightly higher body weight. Male mice 6 to 10 show a bigger decreasing trend in body weight in the first week post-tumor induction compared to male mice 1 to 5. In male mice, also a stabilization of body weight is observed after week three.

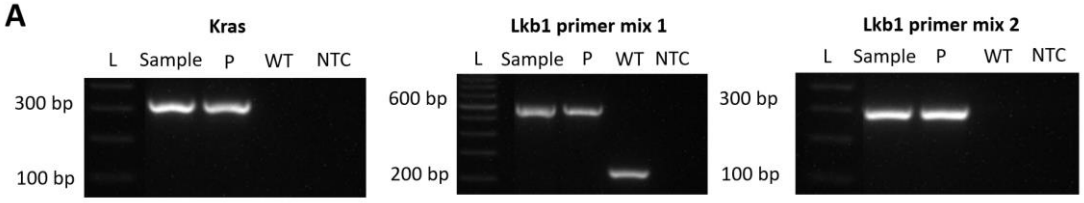

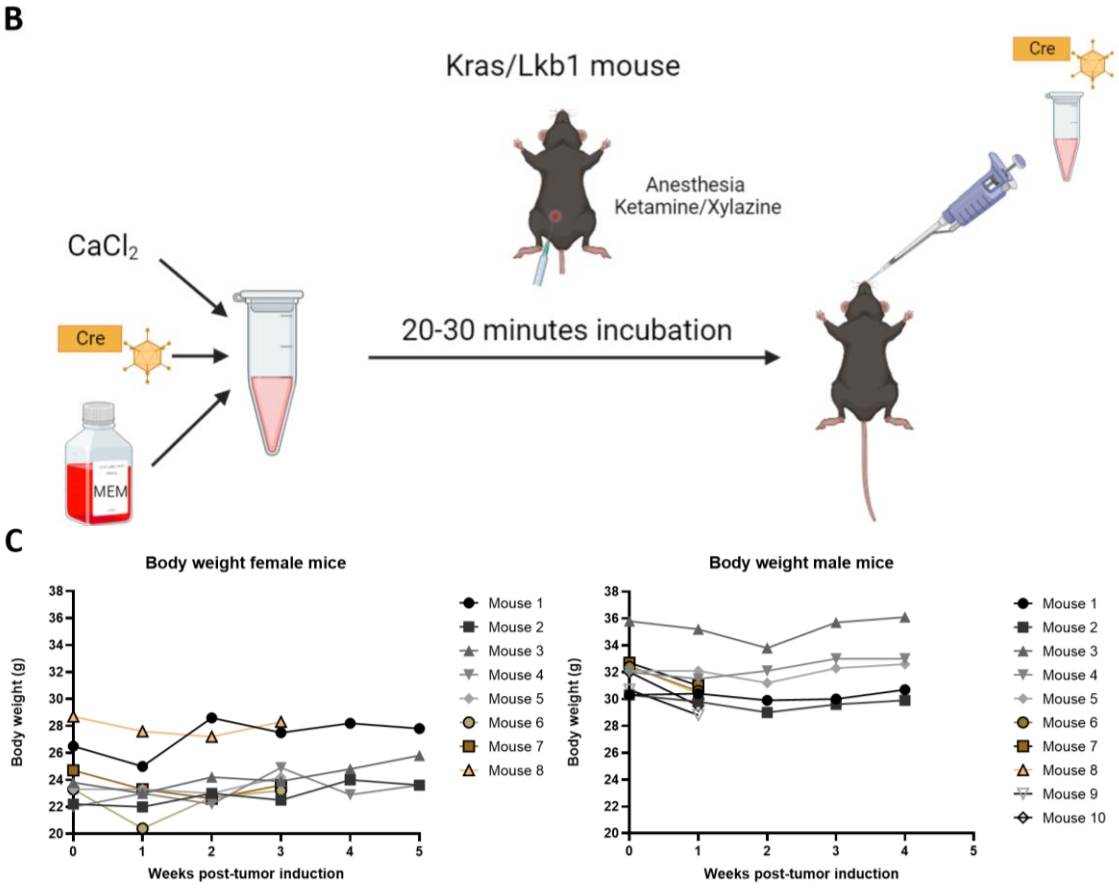

Fig. 2 –Kras/Lkb1 lung cancer mouse model. A) Genotyping of Kras/Lkb1 mouse model to see whether a mouse harbor the genes of interest *(Kras*$^{G12D+/-}$*/Lkb1*$^{-/-}$*)*. Mice that harbor the LoxP-stop-LoxP *Kras* mutation heterozygously show a band at 350 base pair (bp). No band is observed for mice carrying this mutation wild type (WT). Furthermore, Lkb1 primer mix 1 indicates whether the double-floxed *Lkb1* gene is homozygously or heterozygously present. Moreover, it shows whether this is a wild type mouse. The Lkb1 primer mix 2 provides more information regarding the presence of the double-floxed *Lkb1* gene. Consequently, mice that harbor the double-floxed *Lkb1* gene homozygously show a band at 600 bp and 200-300 bp for primer mix 1 and 2, respectively. To ensure correctness of each genotyping experiment, three controls are included: a positive control sample (P), a wild type (WT), and no template control (NTC). **B)** Lung tumor induction in Kras/Lkb1 mouse model. The adenoviral-Cre solution (Ad-Cre) consists of calcium chloride ($CaCl_2$), minimal essential medium (MEM), and adenoviral Cre-recombinase particles. This solution needs to incubate for 20 to 30 min before intranasal administration. **C)** Weekly body weight assessment post-tumor induction. The body weight of mice was measured weekly as an indication to monitor the health condition of mice after lung tumor induction. The weight of the mice at the start of induction is indicated as week 0. The left graph shows the body weight of all induced female mice (n=8) until five weeks post-tumor induction. A big decrease from about 3 g is observed in female mouse 6. Furthermore, an increase of approximately 3 g is seen in female mice 1 and 6 between weeks one and two post-tumor induction. A similar increase is observed in mouse 4 between weeks two and three post-tumor induction. The right graph visualizes the body weight of male mice (n=10) until four weeks after tumor induction. Male mouse 3 has a relative higher body weight compared to the other male mice. Mice 6 to 10 show a bigger decreasing trend in body weight than mice 1 to 5. Male mice have a higher standard body weight compared to female mice. Stabilization of body weight is seen in all male mice and female mouse 1 three weeks after the tumor induction. Additionally, fewer body weight fluctuations were observed in male mice. Overall, all mice show relatively stable body weight.
Kras, Kirsten rat sarcoma; Lkb1, Liver kinase B1.

Optimization of the staining protocol to map the tumor and its microenvironment – First, DAB-based IHC stainings were performed for each marker to test the binding affinity and specificity. (**Fig. 3A**). To visualize the endothelial cells, the CD34 marker was used. A strong signal (brownish precipitate) of CD34 was observed in the blood vessels of the murine lung tissue. Additionally, a lower signal is observed between the alveoli, visualizing the microvessels in the lung. CK7 is tested in renal tissue to indicate epithelial cells. Here, epithelial cells of the loop of Henle are observed with a strong signal. Furthermore, a high signal of the P63 marker was observed in the myoepithelial cells of the prostatic tissue. At last, a lower signal of pancytokeratin is observed in the bronchial epithelium of lung tissue.

To map the tumor and its environment, fluorescent-based multiplex stainings will be performed in future research. Therefore, each marker was also tested in this setting. The results of this experiment are shown in **Fig. 3B**. For CD34 and CK7, the observed fluorescent signal using an Alexa Fluor 555 (AF555) is similar to the observed DAB signal. CD34 is observed in microvessels between the alveoli of the lung, whereas CK7 shows a strong signal in the Loop of Henle of the renal tissue. Furthermore, myoepithelial cells of the prostate are visualized using P63 with AF555. Despite the high signal for this marker in the DAB-IHC setting, a low signal and background fluorescence are observed in the immunofluorescence analysis. For pancytokeratin similar signal is observed in both methods. It showed a lower signal in the bronchial epithelium, using immunocytochemistry, which is also observed when using AF555. The low signal and observed fluorescent background of these last markers indicate the need for further optimization. The settings of the Axio Scan.Z1 Slide scanner (ZEISS) to digitize the IF slides are shown in **Fig. 3C**. In supplemental **Fig S. 2**, the fluorescent signal of vimentin using AF555 is shown. Vimentin is expected to show the stromal cells in the murine colon. However, aspecific bindings are observed in the tubular glands of the murine colon. Therefore, further optimization of this marker is necessary.

Besides the optimization of the cell-specific markers, also different clearing agents were compared to determine the clearing agent that leads to the best quality staining results. Xylene, NeoClear, and UltraClear were compared using both histological and IHC stainings. **Fig. 4A** demonstrates the comparison of the different clearing agents using an H&E staining. Here, Xylene-cleared tissue showed the most bright colors. In contrast, tissue cleared with NeoClear had a lower color intensity, and less contrast is observed between the hematoxylin and eosin stain. Moreover, NeoClear-cleared tissue appears to be more blurry, which makes it difficult to determine the cell morphology. Lastly, tissue cleared with UltraClear, has a higher color intensity than NeoClear-cleared tissue but is still less bright than the Xylene-cleared tissue. Additional to the H&E staining, a TCM staining is executed, visualizing the connective tissue (**Fig. 4B**). Here, the results of the different clearing agents are similar to the results of the H&E staining. Next to the histological stainings, also IHC techniques were used to compare Xylene, NeoClear, and UltraClear. Therefore, two different markers are implemented in this research. Beta 3-tubulin with AF555 is used to visualize nerves. The signal observed for the beta 3-tubulin marker in both DAB-IHC and IF-IHC is similar for Xylene- and NeoClear-cleared tissue (**Fig. 4C**). In contrast, tissue cleared with UltraClear showed a lower intensity for both IHCs. The scan settings for immunofluorescent analysis with beta 3-tubulin vary between the clearing agents since they were set within the range of 5000-7000 for the white value obtaining the best quality images (**Fig. 4E**). The gain of all these digitized slides is the same, whereas the exposure time varies between the different conditions. The exposure time of UltraClear-cleared tissue (80 ms) was higher compared to NeoClear-cleared tissue (70 ms) and lower compared to Xylene-cleared tissue (90 ms). The second marker is podoplanin-Cy3, which indicates the lymph vessels and nodes. **Fig. 4D** shows the IF staining of podoplanin for each clearing condition. Here, for all three clearing agents, the same settings were used when digitizing the slides (**Fig. 4E**). Therefore, correct comparable signals between the clearing agents can be observed. The immunofluorescent staining with podoplanin shows less signal in the Xylene-cleared tissue, but DAPI has a higher intensity for this clearing agent. Additionally, UltraClear-cleared tissue has a lower fluorescent signal compared to the tissue cleared with NeoClear.

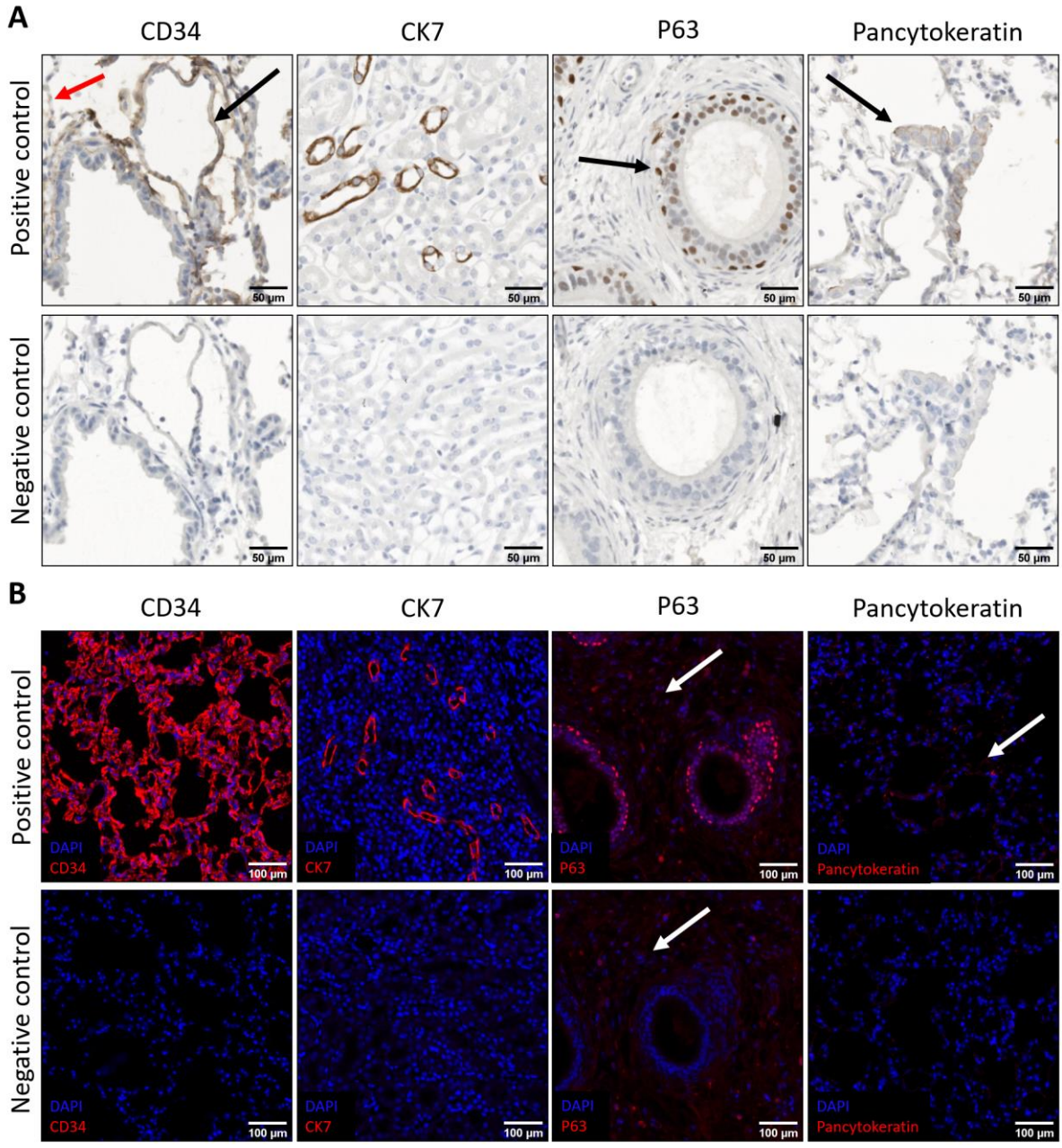

C

	CD34	CK7	P63	Pancytokeratin
DAPI	10% - 60 ms	10% - 60 ms	10% - 60 ms	10% - 60 ms
AF555	70% - 150 ms	40% - 120 ms	40% - 120 ms	100% - 150 ms
Black	81	69	86	150
White	4018	2322	4752	6246

Fig. 3 – Optimization of various markers to map the tumor and its microenvironment in future research. All stainings are performed on murine tissue. **A)** First, a 3,3'-diaminobenzidine (DAB)-based immunohistological (IHC) staining was used to determine the binding affinity and specificity of the primary antibody. CD34 marker indicates the presence of endothelial cells in lung tissue.

A high signal is observed in blood vessels (black arrow), whereas a lower signal shows microvessels in the alveoli (red arrow). Cytokeratin 7 (CK7) shows a high signal for epithelial cells indicating the Loop of Henle in renal tissue. Furthermore, myoepithelial cells in the prostate are visualized using P63. Here, a high signal is observed. Lastly, pancytokeratin shows a lower signal, indicating epithelial cells in the bronchi of the lung. Magnification, 20x. **B)** Immunofluorescent (IF)-based IHC staining to indicate specific cell types. For all fluorescent stainings, an AF555 (red) is used to visualize the different cell types. DAPI (blue) is used as a counterstaining to specify the nuclei. CD34 and CK7 show a fluorescent signal that is similar to the signal seen in the DAB-IHC staining. Although a high signal, using DAB-IHC, is observed for P63, the fluorescent signal is low, and a lot of background fluorescence is present. For pancytokeratin, a very low fluorescent signal is shown. Magnification, 10x. **C)** Settings of the Axio Scan.Z1 Slide scanner (ZEISS) indicating the gain (%) and the exposure time (ms). These settings were used when visualizing the IF-IHC stainings.

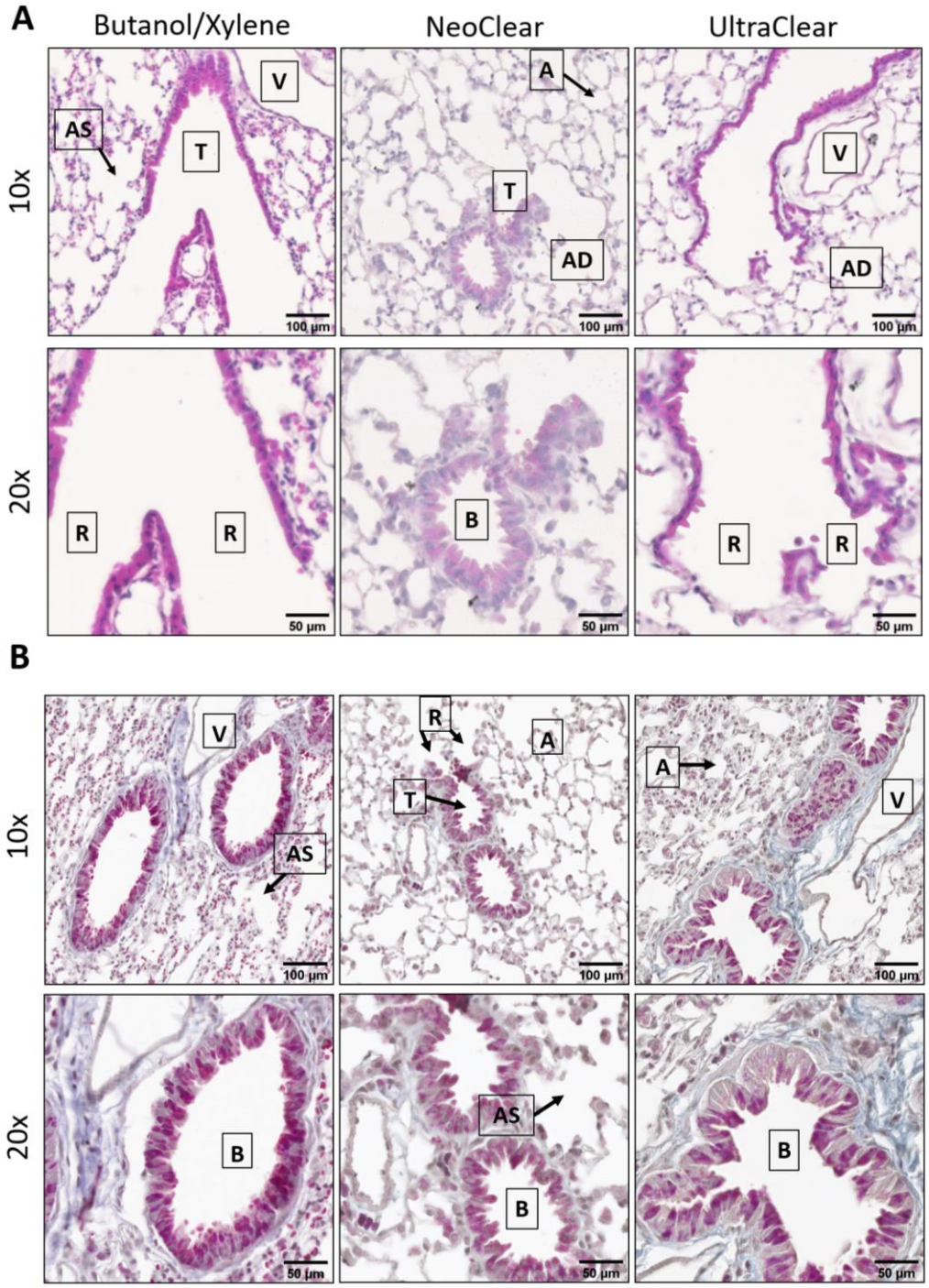

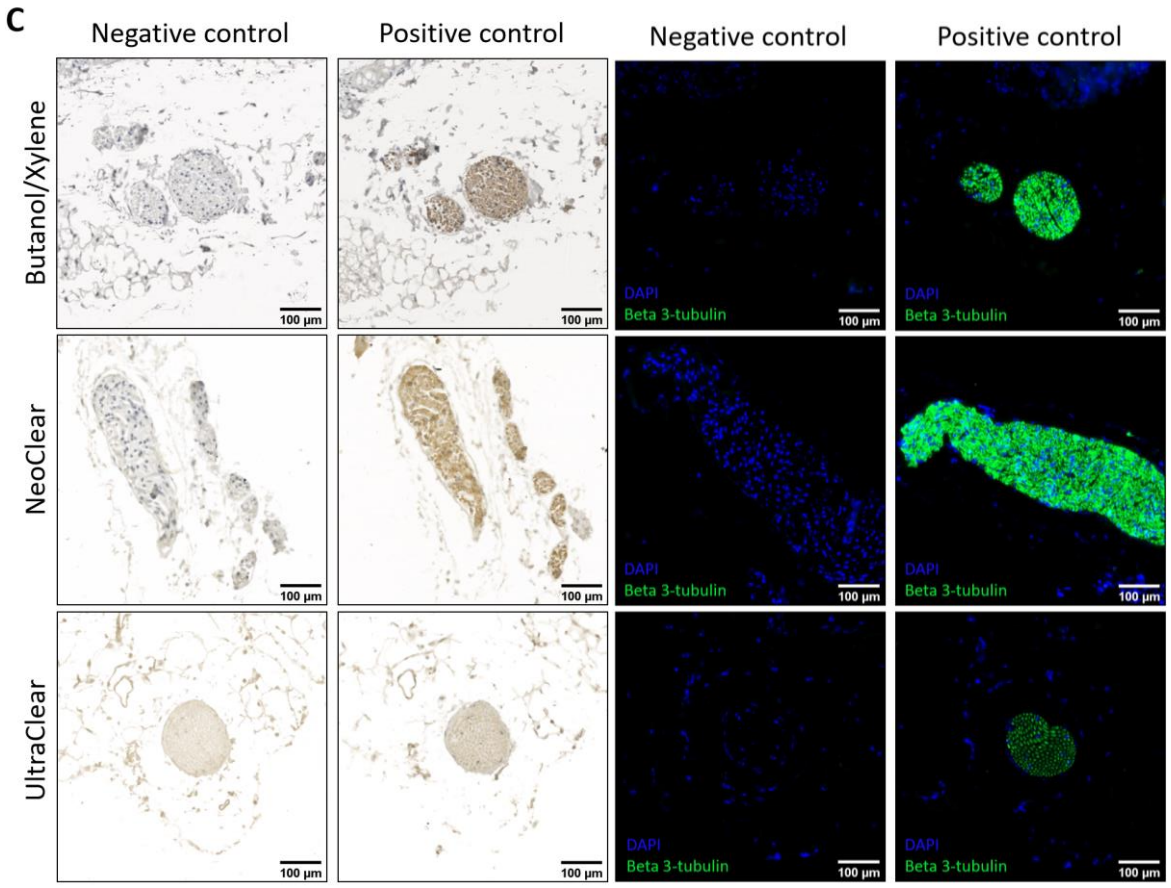
C
Negative control
Positive control
Negative control
Positive control
Butanol/Xylene
NeoClear
UltraClear
DAPI
Beta 3-tubulin
100 µm

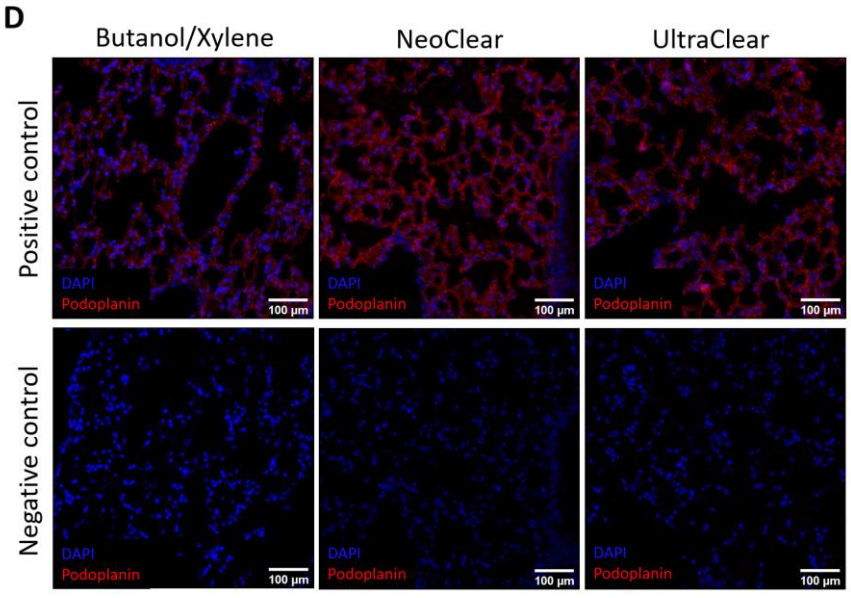
D
Butanol/Xylene
NeoClear
UltraClear
Positive control
Negative control
DAPI
Podoplanin
100 µm

E

	Beta 3-tubulin Xylene (AF488)	Beta 3-tubulin NeoClear (AF488)	Beta 3-Tubulin UltraClear (AF488)	Podoplanin (Cy3)
DAPI	10% - 60 ms	10% - 60 ms	10% - 80 ms	10% - 60 ms
Marker specific channel	50% - 90 ms	50% - 70 ms	50% - 80 ms	50% - 70 ms
Black	1000	1000	1000	60
White	16384	16384	16384	4500

Fig. 4 – The comparison of the effect of different clearing agents using several staining techniques. All stainings are performed on murine lung tissue **A)** Hematoxylin and eosin (H&E) staining. Hematoxylin stains the nucleus blue/purple, whereas eosin stains the cytoplasm and extracellular matrix pink. Xylene-cleared tissue shows brighter colors compared to tissue cleared with UltraClear. This appeared, in its turn, brighter than NeoClear-cleared tissue. Additionally, it is more difficult to observe the cell morphology in tissue cleared with NeoClear. **B)** Masson's Trichrome (TCM) staining. The nucleus is stained with hematoxylin (blue/purple), whereas ponceau (pink/red) is used to stain the cytoplasm and extracellular components. Additionally, aniline blue (blue) indicates connective tissue like collagen fibers. Here, the Xylene-cleared tissue has a higher color intensity compared to UltraClear- and NeoClear-cleared tissue. However, tissue cleared with UltraClear shows brighter colors than NeoClear-cleared tissue. Similar to the H&E staining, the cell morphology in NeoClear-cleared tissue is more vague, making it difficult to distinguish different structures. **C)** Immunohistochemistry (IHC) approaches to visualize nerves using a beta 3-tubulin marker. For the 3,3'-diaminobenzidine (DAB)-based and immunofluorescence (IF)-based IHC staining, the Xylene- and NeoClear-cleared tissue show similar signals. The signal of both immunohistochemical approaches for UltraClear-cleared tissue is less intense compared to the tissue cleared with other clearing agents. In all fluorescent stainings with Alexa Fluor 488 (AF488, green), DAPI (blue) is used as counterstaining to visualize the nuclei. DAPI has a higher signal in NeoClear-cleared tissue compared to than Xylene- and UltraClear-cleared tissue. Magnification, 10x. **D)** IF analysis of podoplanin-Cy3 (red) to indicate the lymph vessels and nodes. Xylene-cleared tissue has a lower intensity than tissue cleared with NeoClear and UltraClear. However, DAPI (blue) shows a brighter signal in the Xylene-cleared tissue compared to the other clearing agents. Magnification, 10x. **E)** Scan settings of the Axio Scan.Z1 Slide scanner (ZEISS) indicating the gain (%) and the exposure time (ms). These settings were used when visualizing the fluorescent stainings. For beta 3-tubulin, different scan settings are used for each clearing agent. The settings were applied for each clearing agent separately when a good signal was observed based on the white value (range 5000-7000). The gain is the same for all clearing agents, whereas the exposure time is higher for Xylene- (90 ms) and UltraClear-cleared tissue (80 ms) compared to tissue cleared with NeoClear (70 ms). Despite the higher exposure time in UltraClear-cleared tissue, the fluorescent signal is low. The scan settings for podoplanin are the same. This leads to a correct comparison of the fluorescent signal observd in the obtained images using different clearing agents.
A, Alveoli; AD, Alveolar duct, AS; Alveolar sac, B, Bronchioli; R, Respiratory bronchioli; T, Terminal bronchioli; V, Vene.

Digitization of human NSCLC samples – Representative cases of the three different human NSCLCs, studied in this research, are shown in **Fig. 5**. A histological difference can be observed between the ADC and SCC, whereas the ADSCC looks like a mix of histological features from both the ADC and SCC (**Fig. 5A**). The ADC has a glandular structure. The bronchioles are lined by densely packed epithelial cells. Furthermore, tumor cells represent a large nucleus with prominent nucleoli. Different immune cells, such as alveolar macrophages and lymphocytes, are present within the ADC. In SCC, which arises from squamous epithelium, polygonal cells with intercellular bridges are observed. Furthermore, keratinization is shown in the form of a keratin pearl. In large SCC, necrosis is also present.

Besides these histological characteristics, immunohistological differences are observed between the ADC and SCC. To visualize different cell type, DAB-IHC stainings were performed in the hospital using various markers. TTF1, CK7, and CK20 are markers that are used to distinguish the ADC. TTF1 and CK7 are expressed in the epithelial cells of the ADC (**Fig. 5B**). Nevertheless, a low TTF1 signal is observed in SCC since this marker is involved in the morphogenesis of the lung. To distinguish the SCC, P40 and P63 are the most commonly used markers. P40 and P63 expression is similar and is observed in myoepithelial cells of the SCC. A low signal of P40 is observed in the ADC epithelial cells.

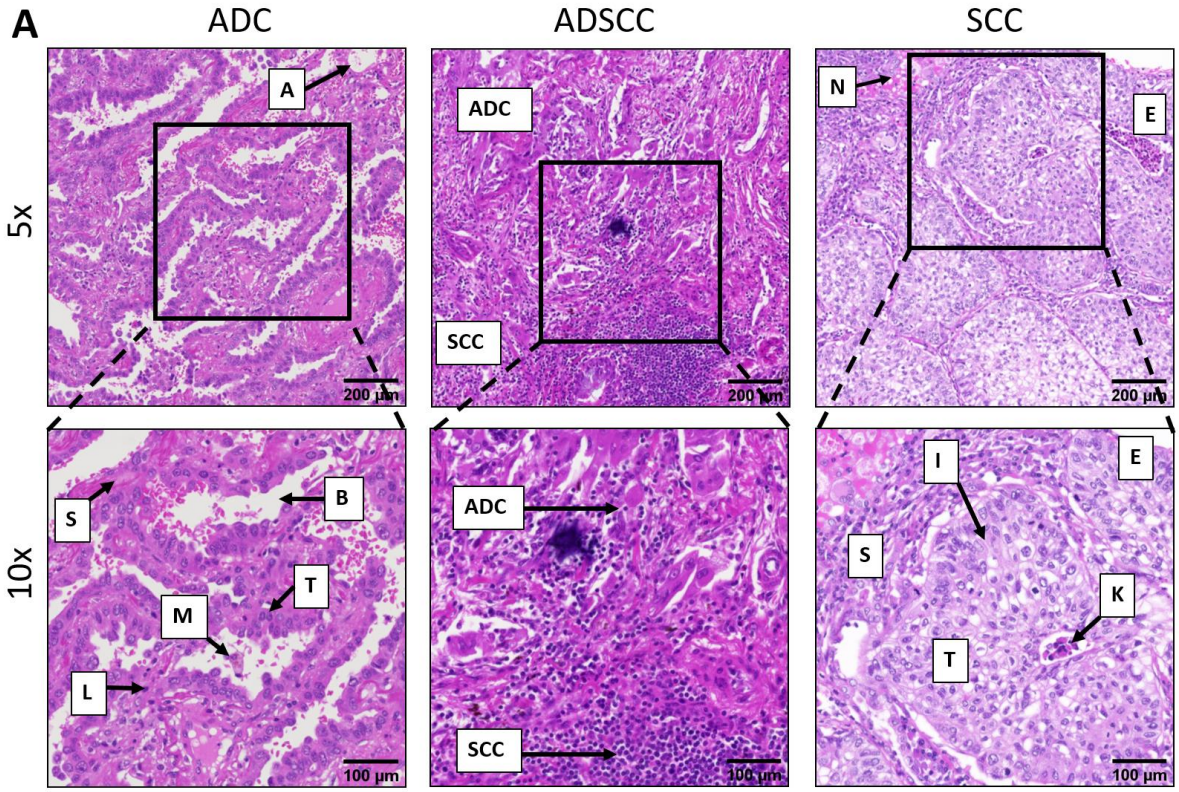

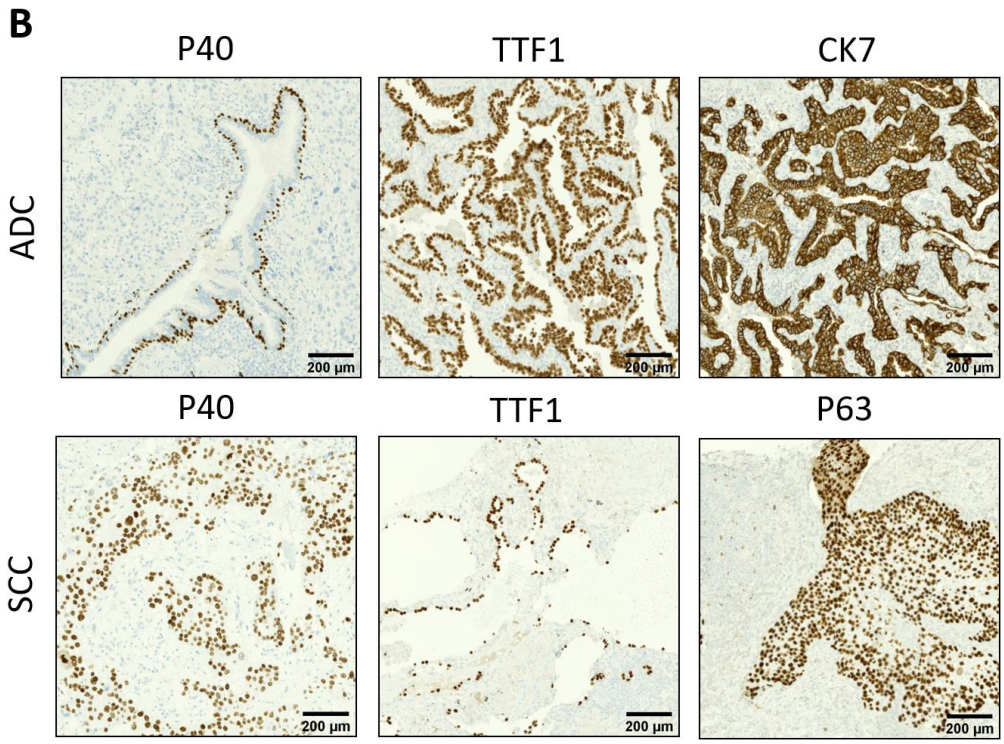

Fig. 5 – **Representative images of human non-small cell lung cancer (NSCLC).** All samples were obtained from human NSCLC patients and digitized using Axio Scan.Z1 Slide scanner (ZEISS). **A)** Hematoxyline and eosin (H&E) staining of adenocarcinoma (ADC), squamous cell carcinoma (SCC), and adenosquamous cell carcinoma (ADSCC). Hematoxylin (blue/purple) indicates the nucleus and eosin (pink) stains the cytoplasm and extracellular matrix. The ADC shows glandular structures. The bronchioli (B) show epithelial cells that are closely arranged. A large nucleus with prominent nucleoli is observed in the tumor cells (T) of ADC. Alveolar macrophages (M) and lymphocytes (L) are shown within the tumor microenvironment. The SCC, derived from squamous epithelial cells, represents polygonal cells with intercellular bridges (I). Moreover, keratine pearls (K) are observed within lung tissue. Here, also necrosis (N) is observed since this is a large SCC. ADSCC, their intermediate form, represents ADC derived as well as SCC-derived tumor cells. **B)** 3,3'-diaminobenzidine (DAB)-based immunohistochemical (IHC) expression of different markers indicating an NSCLC subtype. Thyroid transcription factor 1 (TTF1) and cytokeratin 7 (CK7) are expressed in the epithelial cells of ADC. Despite the fact that these markers are used to distinguish ADC, low expression of TTF1 is observed in SCC due to its involvement in the morphogenesis of the lung. The SCC can be determined using P40 and P63. The expression of these markers in myoepithelial cells is similar in SCC. Here, P40 also shows a low signal in the epithelial cells of ADC. Magnification, 5x. *A, Alveoli; S; Tumor stroma.*

DISCUSSION

NSCLC affects 85% of all lung cancer patients [2]. Regardless of the various treatment options available, they still often fail due to late and insufficient tumor detection [12, 19]. This indicates the need for a potential biomarker to facilitate the diagnostic process and determine a more accurate treatment in a shorter time period. Spatial tumor heterogeneity is known to play a role in cancer progression and treatment response [32]. This will be investigated as a potential biomarker in future research by our group. To determine the spatial tumor heterogeneity, histological and IHC approaches will be used in combination with digital pathology. Therefore, this research aimed to optimize the histological and IHC staining procedures on murine tissue before digitization using WSI. Eventually, this optimization and digitization will lead to the ability to map the heterogeneity of NSCLC tumors and their microenvironment in future research.

First, various markers were tested to indicate the presence of specific cell types. Immunohistological stainings were executed on murine lung tissue and positive control tissue, including the kidney, prostate, and colon, depending on the marker. Optimal results were observed for CD34 on lung tissue and CK7 on renal tissue for both DAB-based and IF-based IHC stainings. Aulakh et al. also described positive results for CD34 using IF techniques (AB81289, dilution 1:500). However, in their research, a higher concentration of this antibody was used to visualized blood cells. Another difference is the use of cryosections in their research whereas our study uses tissue embedded in paraffin [62]. For CK7, similar results for DAB-based IHC staining are accomplished by Drusian et al. using murine renal tissue. However, they did not show any IF-based results for CK7 [63]. Next to CD34 and CK7, also P63 and pancytokeratin showed a strong signal for Dab-IHC stainings in prostatic and lung tissue, respectively. However, for IF analysis, further optimization is necessary for P63, pancytokeratin, and vimentin markers. More specifically, for pancytokeratin, only a low fluorescent signal is observed despite the use of a high concentration (1:50 dilution). A possible optimization step is using an even higher concentration of pancytokeratin or another fluorescent antibody. Martineau et al. showed a high signal for a DAB-IHC approach using sheep lungs. Furthermore, a very low concentration of pancytokeratin (M3515, 1:1000) is used in this study. Nevertheless, they did not show any IF analysis [64]. For P63, a lot of background signal was observed for the FM-IHC approach. Research from Cheng et al. showed similar results in prostatic tissue for the DAB-IHC staining, whereas no results were shown for fluorescent-based stainings [65]. For vimentin aspecific bindings were observed in the murine colon, whereas Wang et al. showed no aspecific fluorescent signal in murine pancreatic tissue. They used a lower concentration of Vimentin (AB5733, 1:500), which can also be implemented in further optimization [66]. At this moment, only a selection of markers has been tested. In the future, more markers will be included to differentiate more cell types in order to determine a potential difference in spatial tumor heterogeneity of the NSCLC subtypes. In the clinical setting, various markers, such as TTF1, CK7, and CK20, are used to differentiate the ADC, whereas P40, P63, and CK5/6 are used to indicate SCC [25, 67]. Therefore, these markers can also be implemented to gain insight into the tumor and its microenvironment. Another marker often used in the diagnosis of NSCLC is programmed cell death ligand 1 (PD-L1), which is a transmembrane protein expressed in cancer cells. Furthermore, it is used in hospitals to predict immunotherapy response using a PD-L1 inhibitor [68, 69]. The binding of lymphocytes to this ligand will result in immunotolerance, indicating the suppression of the T- or B-cell activation, leading to tumor survival [69]. Next to the differentiation between epithelial components of the tumor, immune cells are also an important element of the tumor microenvironment. These cells are essential in cancer initiation and metastasis [70]. Accordingly, markers indicating immune cells will also be implemented in future research to obtain a complete overview of the tumor and its microenvironment. T-lymphocytes are involved in the adaptive immune system. Naïve T-cells eliminate immunogenic cancer cells after activation and migration to the tumor. Furthermore, high T-lymphocyte infiltration correlates with a positive prognosis. However, cancer cells can impair T-cell function, as seen in the binding of T-cells to PD-L1 [68-70]. To distinguish T-cells, CD3 can be used as a marker [71]. Next to T-cells, also B-lymphocytes are present within the tumor microenvironment. These cells promote tumor growth and angiogenesis [70]. For B-lymphocytes, CD19 and

CD20 can be used for all B-cells except plasma cells. These can be visualized using a CD27 marker [72]. Another immune cell type is a macrophage which can be indicated using a CD68 marker. This marker is highly present in alveolar macrophages [73]. Anti-inflammatory macrophages play a role in the removal of cancer cells. However, pro-inflammatory macrophages, developed during cancer progression, promote tumorigenesis [70]. Lastly, neutrophils are immune cells that are initially recruited to the damaged tissue to regulate different processes, such as elimination and inflammation. A high presence of neutrophils corresponds to a poor cancer prognosis [70]. These cells can be visualized using a CXC motif chemokine receptor 2 (CXCR2) marker, an essential chemokine receptor in mice [74].

Besides the optimization of various markers, clearing agents (Xylene, NeoClear, and UltraClear) used in different steps of the staining protocol were also evaluated. In both histological and IHC approaches, these clearing agents were compared to determine which clearing agent resulted in the best quality outcome in several staining procedures. Histological stainings on Xylene-cleared murine lung tissue still showed the most optimal result when comparing the different clearing agents based on the visualized cell morphology. However, Alwahaibi et al. showed optimal results for H&E staining on kidney tissue using UltraClear as a deparaffinization agent. These results were similar to the tissue deparaffinized with Xylene. [46]. For NeoClear, no other results have been published before. The effect of the use of each clearing agent was also evaluated based on IF-IHC analysis. Therefore, beta 3-tubulin and podoplanin were used as immunohistological markers. For the beta 3-tubulin marker, Xylene- and NeoClear-cleared tissue showed similar signals for both DAB-based and FM-based IHC, while tissue cleared with UltraClear showed lower signals. However, it is important to notice that the settings for AF488, using a beta 3-tubulin marker, are not the same for each clearing agent. The gain was constant for each clearing agent, while the exposure time was the highest for Xylene-cleared tissue and the lowest for NeoClear-cleared tissue. Consequently, this means that NeoClear-cleared tissue has a similar signal as Xylene-cleared tissue, while the exposure time was shorter. Also, for UltraClear-cleared tissue, a lower signal is observed when having a longer exposure time compared to tissue cleared with NeoClear. In contrast to beta 3-tubulin, for the podoplanin marker the same scan settings were used for all clearing agent. This indicates the correct comparison of the visible signal observed on the scan. The signal for podoplanin was higher in NeoClear-cleared tissue compared to tissue cleared with Xylene and UltraClear. In this study, deparaffinization was performed using each clearing agent two times for five minutes. Similarly, Alwahaibi et al. also used UltraClear two times to deparaffinize the tissue. However, no exact times were appointed. A possible difference in this deparaffinization time could explain the variation in results. Moreover, they only compared the used Xylene vs. UltraClear based on H&E staining; no other staining methods were tested [46]. According to the manufacturer's protocol for NeoClear, it is stated that two times five minutes should be sufficient for optimal staining [75]. However, applying this protocol, the expected results were not observed. Thus, further optimization by extending the incubation time of NeoClear can be studied. These safer alternatives may have more difficulties impregnating the tissue since it is a less concentrated agent than Xylene, assuming these products needs a longer time before optimal functioning. [46]. This could indicate the need for a longer deparaffinization time, which can be tested in further experiments. Deparaffinization times can be increased up to two times, about ten, 20, and 30 minutes for each clearing agent.

After optimization of the staining protocol, multiplex stainings can be performed in future research. This will lead to more insight into the presence and organization of these different cell types simultaneously in the same tissue slide. When performing this technique, the goal of the cell-specific markers needs to be considered. The strength and area of the expression must be taken into account. Furthermore, the choice of primary antibody is crucial since different antibodies need to have another host to avoid aspecific bindings of the secondary antibody [76]. The emission and excitation spectra of the fluorescent secondary antibody can only minimally overlap between various markers [77]. Panels with four different markers can be composed. For example, an immune cell panel can be made with CD3 (T-lymphocytes), CD19 (B-lymphocytes, CD68 (macrophages), CXCR2 (neutrophils), which map all the immune cells in the tumor microenvironment. Different panels will be used

on lung tumor tissue from the preclinical mouse model to determine spatial tumor heterogeneity using digital pathology. Currently, no optimal staining protocol is achieved for scanning the slides using WSI.

When achieving an optimal staining protocol, the stainings will be performed on lung tumor tissue isolated from the Kras/Lkb1 mouse model. At this moment, no lung tumor tissue has been obtained yet, but the mice are already induced with Ad-Cre to develop lung cancer. To monitor the health status of these mice post-tumor induction, the body weight was assessed weekly. The body weight of all mice is relatively stable. However, some mice have fluctuations in their body weight. Female mouse 6 lost almost 3 g in one week, and whereafter, this mouse gained about 3 g in the second week. These body weight fluctuations could be explained by several factors. The assessment of the body weight needs to be performed in a flow cabinet because of biosafety reasons, whereby the airflow as well as the movement of stressed animals, can influence the accuracy of the measurement. However, measuring the body weight only is not sufficient to monitor the health status of the animal. Besides body weight assessment, it is important to follow up on the physical condition of each mouse. As a result of the tumor formation, the body weight can increase while fat and muscles break down [78]. Therefore, the body condition scoring (BCS) system is a more sensitive and accurate measurement of animal welfare. This BCS uses a scoring system from 1 to 5, indicating emaciation and obesity, respectively (**Fig S. 3**). Scoring with this system is performed by passing a finger over the sacroiliac bones. A score of 3 is considered optimal, meaning in good health condition. This scoring system is quick, reliable, and relatively easy to use [78].

In addition to the murine tumor tissue, also human tissue samples were provided. H&E samples from 70 patients were digitized using WSI. The gold standard used in the classification of NSCLC subtypes is H&E stainings. Here, tumor heterogeneity in the form of differences in morphological structures is used to distinguish the subtypes. However, it is recommended to evaluate the subtypes using the specific ADC and SCC markers since many NSCLC samples present variations in their IHC profile [79]. Li et al. used single-cell RNA sequencing to investigate a difference in tumor heterogeneity in NSCLC to provide a more accurate treatment plan based on this tumor heterogeneity [80].

In future research, murine lung tumors will be used to visualize different specific cell types simultaneously using multiplex stainings. Analysis of the spatial tumor heterogeneity will be assessed using AI tools. These techniques can also be applied to human NSCLC samples. At first, spatial tumor heterogeneity can be linked to the survival of patients. Afterward, differences in treatment plans and the heterogeneity profile of patients with NSCLC can be related to the treatment response. This indicates the potential use of spatial tumor heterogeneity as a biomarker in NSCLC.

CONCLUSION

In conclusion, our results suggest the establishment of the re-evaluation and optimization of the general IHC protocol. However, further optimization for the use of safer clearing agents such as NeoClear and UltraClear is necessary. Furthermore, the use of some cell-specific markers like P63, pancytokeratin and vimentin as well as additional markers need to be optimized. An optimal staining procedure will contribute to obtaining high quality images using WSI. In future research, analysis of spatial tumor heterogeneity and the development of an AI tool can lead to the use of spatial tumor heterogeneity as a potential biomarker for NSCLC. This potential biomarker can provide a more accurate diagnosis and an appropriate therapy in a shorter time period. Finally, a new form of personalized medicine can be established for NSCLC patients.

REFERENCES

1. Gridelli C, Rossi A, Carbone DP, Guarize J, Karachaliou N, Mok T, et al. Non-small-cell lung cancer. Nat Rev Dis Primers. 2015;1:15009.
2. Siddiqui F, Vaqar S, Siddiqui AH. Lung Cancer. StatPearls. Treasure Island (FL)2023.
3. WHO. Cancer 2022 [Available from: https://www.who.int/news-room/fact-sheets/detail/cancer.
4. Belgium.be. Causes of premature death 2022 [Available from: https://www.healthybelgium.be/en/health-status/mortality-and-causes-of-death/causes-of-premature-death.
5. Myers DJ, Wallen JM. Lung Adenocarcinoma. StatPearls. Treasure Island (FL)2023.
6. Naeem Z. Second-hand smoke - ignored implications. Int J Health Sci (Qassim). 2015;9(2):V-VI.
7. de Alencar VTL, Formiga MN, de Lima VCC. Inherited lung cancer: a review. Ecancermedicalscience. 2020;14:1008.
8. Cooper WA, Lam DC, O'Toole SA, Minna JD. Molecular biology of lung cancer. J Thorac Dis. 2013;5 Suppl 5(Suppl 5):S479-90.
9. Basumallik N, Agarwal M. Small Cell Lung Cancer. StatPearls. Treasure Island (FL)2023.
10. Li C, Lu H. Adenosquamous carcinoma of the lung. Onco Targets Ther. 2018;11:4829-35.
11. Han X, Li F, Fang Z, Gao Y, Li F, Fang R, et al. Transdifferentiation of lung adenocarcinoma in mice with Lkb1 deficiency to squamous cell carcinoma. Nat Commun. 2014;5:3261.
12. Non-Small Cell Lung Cancer Treatment (PDQ(R)): Health Professional Version. PDQ Cancer Information Summaries. Bethesda (MD)2002.
13. Bio M. What are the Differences Between Small Cell and Non-Small Cell Lung Cancer? 2023 [Available from: https://massivebio.com/what-are-the-differences-between-small-cell-and-non-small-cell-lung-cancer/.
14. Xie X, Li X, Tang W, Xie P, Tan X. Primary tumor location in lung cancer: the evaluation and administration. Chin Med J (Engl). 2021;135(2):127-36.
15. Solis LM, Behrens C, Raso MG, Lin HY, Kadara H, Yuan P, et al. Histologic patterns and molecular characteristics of lung adenocarcinoma associated with clinical outcome. Cancer. 2012;118(11):2889-99.
16. Mullangi S, Lekkala MR. Adenocarcinoma. StatPearls. Treasure Island (FL)2023.
17. Sabbula BR, Gasalberti DP, Anjum F. Squamous Cell Lung Cancer. StatPearls. Treasure Island (FL)2023.
18. Suarez E, Knollmann-Ritschel BEC. Squamous Cell Carcinoma of the Lung. Acad Pathol. 2017;4:2374289517705950.
19. Zappa C, Mousa SA. Non-small cell lung cancer: current treatment and future advances. Transl Lung Cancer Res. 2016;5(3):288-300.
20. Nooreldeen R, Bach H. Current and Future Development in Lung Cancer Diagnosis. Int J Mol Sci. 2021;22(16).
21. Morrison LE, Lefever MR, Lewis HN, Kapadia MJ, Bauer DR. Conventional histological and cytological staining with simultaneous immunohistochemistry enabled by invisible chromogens. Lab Invest. 2022;102(5):545-53.
22. Affandi KA, Tizen NMS, Mustangin M, Zin R. p40 Immunohistochemistry Is an Excellent Marker in Primary Lung Squamous Cell Carcinoma. J Pathol Transl Med. 2018;52(5):283-9.
23. Verset L, Arvanitakis M, Loi P, Closset J, Delhaye M, Remmelink M, et al. TTF-1 positive small cell cancers: Don't think they're always primary pulmonary! World J Gastrointest Oncol. 2011;3(10):144-7.
24. Guan L, Zhao X, Tang L, Chen J, Zhao J, Guo M, et al. Thyroid Transcription Factor-1: Structure, Expression, Function and Its Relationship with Disease. Biomed Res Int. 2021;2021:9957209.
25. Luo HT, Liang CX, Luo RC, Gu WG. Identification of relevant prognostic values of cytokeratin 20 and cytokeratin 7 expressions in lung cancer. Biosci Rep. 2017;37(6).
26. NIH. KRT7 keratin 7 [Homo sapiens (human)] 2023.
27. Smirnov A, Anemona L, Novelli F, Piro CM, Annicchiarico-Petruzzelli M, Melino G, et al. p63 Is a Promising Marker in the Diagnosis of Unusual Skin Cancer. Int J Mol Sci. 2019;20(22).
28. Moses MA, George AL, Sakakibara N, Mahmood K, Ponnamperuma RM, King KE, et al. Molecular Mechanisms of p63-Mediated Squamous Cancer Pathogenesis. Int J Mol Sci. 2019;20(14).

29. : National Cancer Institute 2023. Tumor Heterogeneity
30. Janku F. Tumor heterogeneity in the clinic: is it a real problem? Ther Adv Med Oncol. 2014;6(2):43-51.
31. Yuan Y. Spatial Heterogeneity in the Tumor Microenvironment. Cold Spring Harb Perspect Med. 2016;6(8).
32. Wu HJ, Temko D, Maliga Z, Moreira AL, Sei E, Minussi DC, et al. Spatial intra-tumor heterogeneity is associated with survival of lung adenocarcinoma patients. Cell Genom. 2022;2(8).
33. Ramon YCS, Sese M, Capdevila C, Aasen T, De Mattos-Arruda L, Diaz-Cano SJ, et al. Clinical implications of intratumor heterogeneity: challenges and opportunities. J Mol Med (Berl). 2020;98(2):161-77.
34. Zhu L, Jiang M, Wang H, Sun H, Zhu J, Zhao W, et al. A narrative review of tumor heterogeneity and challenges to tumor drug therapy. Ann Transl Med. 2021;9(16):1351.
35. Chervoneva I, Peck AR, Yi M, Freydin B, Rui H. Quantification of spatial tumor heterogeneity in immunohistochemistry staining images. Bioinformatics. 2021;37(10):1452-60.
36. Rajkovic N, Li X, Plataniotis KN, Kanjer K, Radulovic M, Milosevic NT. The Pan-Cytokeratin Staining Intensity and Fractal Computational Analysis of Breast Tumor Malignant Growth Patterns Prognosticate the Occurrence of Distant Metastasis. Front Oncol. 2018;8:348.
37. Menz A, Gorbokon N, Viehweger F, Lennartz M, Hube-Magg C, Hornsteiner L, et al. Pan-keratin Immunostaining in Human Tumors: A Tissue Microarray Study of 15,940 Tumors. Int J Surg Pathol. 2022:10668969221117243.
38. Lin G, Finger E, Gutierrez-Ramos JC. Expression of CD34 in endothelial cells, hematopoietic progenitors and nervous cells in fetal and adult mouse tissues. Eur J Immunol. 1995;25(6):1508-16.
39. Sidney LE, Branch MJ, Dunphy SE, Dua HS, Hopkinson A. Concise review: evidence for CD34 as a common marker for diverse progenitors. Stem Cells. 2014;32(6):1380-9.
40. Roda N, Blandano G, Pelicci PG. Blood Vessels and Peripheral Nerves as Key Players in Cancer Progression and Therapy Resistance. Cancers (Basel). 2021;13(17).
41. NIH. TUBB3 tubulin beta 3 class III [Homo sapiens (human)] 2023.
42. Krishnan H, Rayes J, Miyashita T, Ishii G, Retzbach EP, Sheehan SA, et al. Podoplanin: An emerging cancer biomarker and therapeutic target. Cancer Sci. 2018;109(5):1292-9.
43. Pereira ER, Jones D, Jung K, Padera TP. The lymph node microenvironment and its role in the progression of metastatic cancer. Semin Cell Dev Biol. 2015;38:98-105.
44. Gurina TS, Simms L. Histology, Staining. StatPearls. Treasure Island (FL)2023.
45. Alwahaibi N, Aljaradi S, Alazri H. Alternative to xylene as a clearing agent in histopathology. J Lab Physicians. 2018;10(2):189-93.
46. Alwahaibi NY, Aldughaishi SH. A substitute to xylene in deparaffinization and clearing prior to coverslipping in histopathology. J Lab Physicians. 2019;11(2):118-22.
47. Avantor V. Xylene substitute, Neo-Clear®, Sigma-Aldrich® 2023 [Available from: https://be.vwr.com/store/product/nl/11919767/xylene-substitute-neo-clear-sigma-aldrich.
48. Zhang H, Fillmore Brainson C, Koyama S, Redig AJ, Chen T, Li S, et al. Lkb1 inactivation drives lung cancer lineage switching governed by Polycomb Repressive Complex 2. Nat Commun. 2017;8:14922.
49. Chevallier M, Borgeaud M, Addeo A, Friedlaender A. Oncogenic driver mutations in non-small cell lung cancer: Past, present and future. World J Clin Oncol. 2021;12(4):217-37.
50. Westcott PM, To MD. The genetics and biology of KRAS in lung cancer. Chin J Cancer. 2013;32(2):63-70.
51. NIH. KRAS KRAS proto-oncogene GTPase [Homo sapiens (human)]. 2023.
52. Adderley H, Blackhall FH, Lindsay CR. KRAS-mutant non-small cell lung cancer: Converging small molecules and immune checkpoint inhibition. EBioMedicine. 2019;41:711-6.
53. Mao Z, Xiao H, Shen P, Yang Y, Xue J, Yang Y, et al. KRAS(G12D) can be targeted by potent inhibitors via formation of salt bridge. Cell Discov. 2022;8(1):5.
54. Ndembe G, Intini I, Perin E, Marabese M, Caiola E, Mendogni P, et al. LKB1: Can We Target an Hidden Target? Focus on NSCLC. Front Oncol. 2022;12:889826.
55. NIH. STK11 serine/threonine kinase 11 [Homo sapiens (human)]. 2023.
56. Bonanno L, Zulato E, Pavan A, Attili I, Pasello G, Conte P, et al. LKB1 and Tumor Metabolism: The Interplay of Immune and Angiogenic Microenvironment in Lung Cancer. Int J Mol Sci. 2019;20(8).

57. Ji H, Ramsey MR, Hayes DN, Fan C, McNamara K, Kozlowski P, et al. LKB1 modulates lung cancer differentiation and metastasis. Nature. 2007;448(7155):807-10.
58. Tian X, Zhou B. Strategies for site-specific recombination with high efficiency and precise spatiotemporal resolution. J Biol Chem. 2021;296:100509.
59. Baxi V, Edwards R, Montalto M, Saha S. Digital pathology and artificial intelligence in translational medicine and clinical practice. Mod Pathol. 2022;35(1):23-32.
60. Dexter A, Tsikritsis D, Belsey NA, Thomas SA, Venton J, Bunch J, et al. Next Generation Digital Pathology: Emerging Trends and Measurement Challenges for Molecular Pathology. Journal of Molecular Pathology 2022.
61. DuPage M, Dooley AL, Jacks T. Conditional mouse lung cancer models using adenoviral or lentiviral delivery of Cre recombinase. Nat Protoc. 2009;4(7):1064-72.
62. Aulakh GK, Maltare S, Khanh LNP, Singh B. CD34 protein is expressed in murine, canine, and porcine lungs. Can J Vet Res. 2021;85(3):161-9.
63. Drusian L, Nigro EA, Mannella V, Pagliarini R, Pema M, Costa ASH, et al. mTORC1 Upregulation Leads to Accumulation of the Oncometabolite Fumarate in a Mouse Model of Renal Cell Carcinoma. Cell Rep. 2018;24(5):1093-104 e6.
64. Martineau HM, Cousens C, Imlach S, Dagleish MP, Griffiths DJ. Jaagsiekte sheep retrovirus infects multiple cell types in the ovine lung. J Virol. 2011;85(7):3341-55.
65. Cheng S, Prieto-Dominguez N, Yang S, Connelly ZM, StPierre S, Rushing B, et al. The expression of YAP1 is increased in high-grade prostatic adenocarcinoma but is reduced in neuroendocrine prostate cancer. Prostate Cancer Prostatic Dis. 2020;23(4):661-9.
66. Wang YJ, McAllister F, Bailey JM, Scott SG, Hendley AM, Leach SD, et al. Dicer is required for maintenance of adult pancreatic acinar cell identity and plays a role in Kras-driven pancreatic neoplasia. PLoS One. 2014;9(11):e113127.
67. Inamura K. Update on Immunohistochemistry for the Diagnosis of Lung Cancer. Cancers (Basel). 2018;10(3).
68. Teixido C, Vilarino N, Reyes R, Reguart N. PD-L1 expression testing in non-small cell lung cancer. Ther Adv Med Oncol. 2018;10:1758835918763493.
69. Wu Y, Chen W, Xu ZP, Gu W. PD-L1 Distribution and Perspective for Cancer Immunotherapy-Blockade, Knockdown, or Inhibition. Front Immunol. 2019;10:2022.
70. Gonzalez H, Hagerling C, Werb Z. Roles of the immune system in cancer: from tumor initiation to metastatic progression. Genes Dev. 2018;32(19-20):1267-84.
71. Sauls RS, McCausland C, Taylor BN. Histology, T-Cell Lymphocyte. StatPearls. Treasure Island (FL)2023.
72. Althwaiqeb SA, Bordoni B. Histology, B Cell Lymphocyte. StatPearls. Treasure Island (FL)2023.
73. Wang C, Xie J, Zhao L, Fei X, Zhang H, Tan Y, et al. Alveolar macrophage dysfunction and cytokine storm in the pathogenesis of two severe COVID-19 patients. EBioMedicine. 2020;57:102833.
74. Delobel P, Ginter B, Rubio E, Balabanian K, Lazennec G. CXCR2 intrinsically drives the maturation and function of neutrophils in mice. Front Immunol. 2022;13:1005551.
75. Millipore M. Neo-Clear 2023 [Available from: https://www.merckmillipore.com/BE/fr/product/Neo-Clear,MDA_CHEM-109843#documentation.
76. Buchwalow I, Samoilova V, Boecker W, Tiemann M. Multiple immunolabeling with antibodies from the same host species in combination with tyramide signal amplification. Acta Histochem. 2018;120(5):405-11.
77. Hofman P, Badoual C, Henderson F, Berland L, Hamila M, Long-Mira E, et al. Multiplexed Immunohistochemistry for Molecular and Immune Profiling in Lung Cancer-Just About Ready for Prime-Time? Cancers (Basel). 2019;11(3).
78. Burkholder T, Foltz C, Karlsson E, Linton CG, Smith JM. Health Evaluation of Experimental Laboratory Mice. Curr Protoc Mouse Biol. 2012;2:145-65.
79. Bernardi FDC, Bernardi MDC, Takagaki T, Siqueira SAC, Dolhnikoff M. Lung cancer biopsy: Can diagnosis be changed after immunohistochemistry when the H&E-Based morphology corresponds to a specific tumor subtype? Clinics (Sao Paulo). 2018;73:e361.
80. Li Q, Wang R, Yang Z, Li W, Yang J, Wang Z, et al. Molecular profiling of human non-small cell lung cancer by single-cell RNA-seq. Genome Med. 2022;14(1):87.

Acknowledgements – CD acknowledges Biomedical Research Center BIOMED (Hasselt University) for her senior internship. CD is grateful for the internship allocation in FIERCE lab, concerning research in the field of oncology. KN is thanked for the excellent daily supervision and pleasant collaboration during this internship. CD is thankfull for all the techniques learned from KN. EW is acknowledged for the overall support during this period. Furthermore, Jeroen Bogie is thanked for the feedback and suggestions during the intermediate evaluations. Lastly, CD would like to thank her family and friends for their unconditional support during this internship and the overall educational experience.

Author contributions – EW together with the collaboration from Data Science Institute of Hasselt University (DSI) and Limburg Clinical Research Center (LCRC) conceived and designed the research. CD and Amber Theunissen performed all the experiments with guidance and support of KN. KN provided assistance in the digitization of all tissue slides. CD wrote the thesis in collaboration with KN, who gave feedback and feedforward. All authors carefully edited the manuscript.

SUPPLEMENTARY TABLES AND FIGURES

Table S. 1 – Overview of the used fluorescent secondary antibodies (sAB) to visualize specific cell types.

Primary AB	Secondary AB	Dilution (sAB)	Reference (sAB)
Beta 3-tubulin	AF488	1:300	A11017 Invitrogen
CD34	AF555	1:300	A21430 Invitrogen
CK7	AF555	1:300	A21430 Invitrogen
P63	AF555	1:300	A21425 Invitrogen
Pancytokeratin (ae1/ae3)	AF555	1:50	A21425 Invitrogen
Podoplanin	Cy3	1:300	107-166-142 Jackson ImmunoResearch
Vimentin	AF647	1:300	703-605-155 Jackson ImmunoResearch

AB, Antibody; AF, Alexa Fluor; CK, Cytokeratin.

Table S. 2 – Overview of the used secondary antibodies (sAB) conjugated with Horseradish peroxidase (HRP) to assess the binding affinity and specificity of the primary antibody.

Primary AB	Secondary AB	Dilution (sAB)	Reference (sAB) - DAKO
Beta 3-tubulin	Rb α M (biotynilated) Streptavidin - HRP	1:400 1:400	E0413 P0397
CD34	G α Rb - HRP	1:400	P0448
CK7	G α Rb - HRP	1:400	P0448
P63	Rb α M (biotynilated) Streptavidin – HRP	1:400 1:400	E0413 P0397
Pancytokeratin (ae1/ae3)	Rb α M (biotynilated) Streptavidin - HRP	1:400 1:400	E0413 P0397

α, anti; AB, Antibody; CK, Cytokeratin; G, Goat; M, Mouse; Rb, Rabbit.

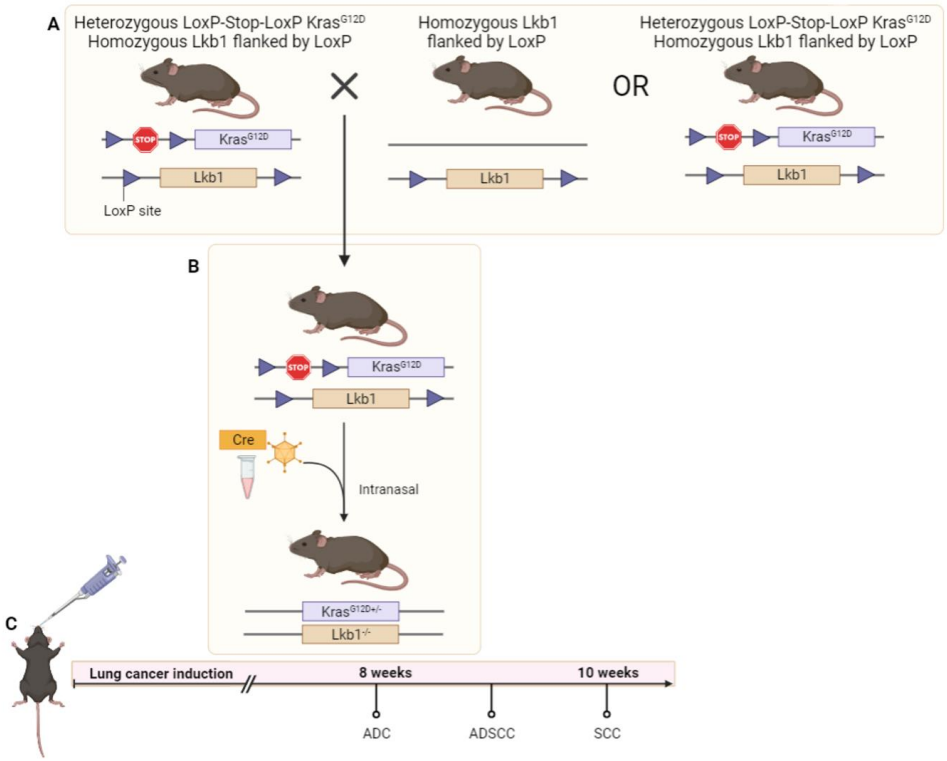

Fig S. 1 – Experimental set-up of preclinical Kras/Lkb1 mouse model. A) Breeding of the Kras/Lkb1 mouse model. Offspring with the correct genotype ($Kras^{G12D+/-}/Lkb1^{-/-}$) will be used for further experiments. **B)** Lung cancer will be induced through the intranasal administration of adenoviral Cre-recombinase particles in solution (Ad-Cre). This results in the expression of the heterozygous *Kras* ($Kras^{G12D+/-}$) mutation and homozygous *Lkb1* deficiency ($Lkb1^{-/-}$) that on their turn will initiate tumorigenesis. **C)** An overview of the timeline post-intranasal administration of Ad-Cre. Adenocarcinoma (ADC), adenosquamous cell carcinoma (ADSCC), and squamous cell carcinoma (SCC) development occur at eight weeks, between eight and ten weeks, and ten weeks after tumor induction, respectively, as described by Ji et al. [57]. *Kras, Kirsten rat sarcoma; Lkb1, Liver kinase B1. Figure made in BioRender.*

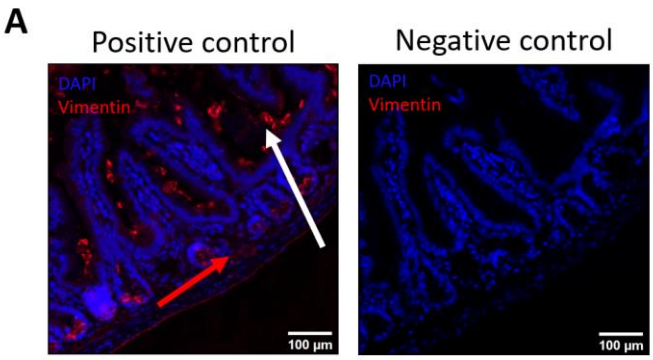

B

	Vimentin
DAPI	10% - 50 ms
AF647	10% - 70 ms
Black	75
White	3617

Fig S. 2 – **Immunofluorescent (IF)-based immunohistochemical (IHC) staining of vimentin.** Vimentin in combination with Alexa Fluor 647 (AF647, red) is used to specify stromal cells in the murine colon. Aspecific signal is observed within the tubular glands (white arrow). However, fluorescent signal is expected in lamina propria of the colon (red arrow). Despite the aspecific bindings, no signal is observed in the negative control. Magnification, 10x. **B)** Settings of the Axio Scan.Z1 Slide scanner (ZEISS) used to obtain digitized slides indicating the gain (%) and the exposure time (ms) as well as black and white value settings to acquire images (A).

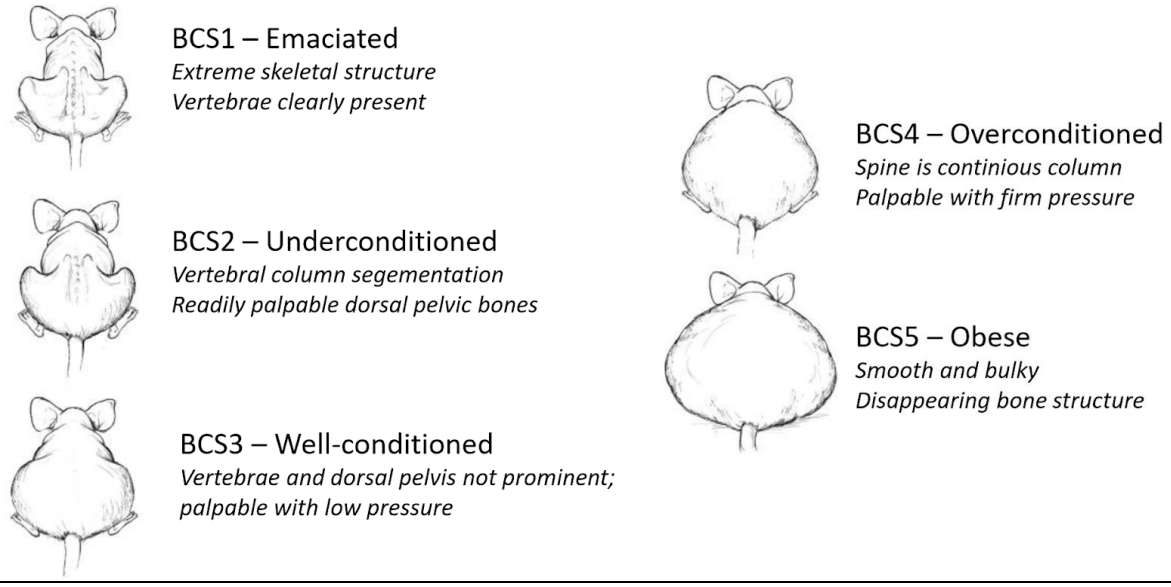

Fig S. 3 – **Body condition scoring (BCS) system.** This scoring system is another method to assess the health condition of the mice. Mice can be scored by passing a finger over the sacroiliac bones and determine the BCS score ranging from 1 to 5. *Figure adapted from Burkholder et al. [78].*